

Direct Learning of Mesh and Appearance via 3D Gaussian Splatting

Ancheng Lin and Jun Li

School of Computer Science, Australian Artificial Intelligence Institute (AII),
University of Technology Sydney, Sydney, NSW 2007, Australia

ancheng.lin@student.uts.edu.au

jun.li@uts.edu.au

Abstract. Accurately reconstructing a 3D scene including explicit geometry information is both attractive and challenging. Geometry reconstruction can benefit from incorporating differentiable appearance models, such as Neural Radiance Fields and 3D Gaussian Splatting (3DGS). In this work, we propose a learnable scene model that incorporates 3DGS with an explicit geometry representation, namely a mesh. Our model learns the mesh and appearance in an end-to-end manner, where we bind 3D Gaussians to the mesh faces and perform differentiable rendering of 3DGS to obtain photometric supervision. The model creates an effective information pathway to supervise the learning of the scene, including the mesh. Experimental results demonstrate that the learned scene model not only achieves state-of-the-art rendering quality but also supports manipulation using the explicit mesh. In addition, our model has a unique advantage in adapting to scene updates, thanks to the end-to-end learning of both mesh and appearance.

Keywords: 3D reconstruction · Gaussian splatting · Hybrid representation · Mesh-guided manipulation

1 Introduction

Meshes carrying explicit geometric information are often the preferred choice in numerous geometry processing scenarios. When building a 3D scene model that includes a mesh, gradient-based optimization from visual observation is challenging due to the complicated pipeline required to produce the synthetic views. Recently, neural surface reconstruction methods [27, 31] represent scene geometry as an implicit signed distance function (SDF) and establish a connection with Neural Radiance Fields (NeRFs) [17], enabling effective image-based supervision. However, the geometry is learned indirectly from the radiance field and faces the challenge of expensive ray-marching in the volumetric rendering of NeRFs.

3D Gaussian Splatting (3DGS) [14] has recently gained popularity due to its ability to render photorealistic images significantly faster than NeRFs. Despite the advantages in rendering quality and speed, learning a mesh using 3DGS remains problematic due to the misalignment between the Gaussian centers and

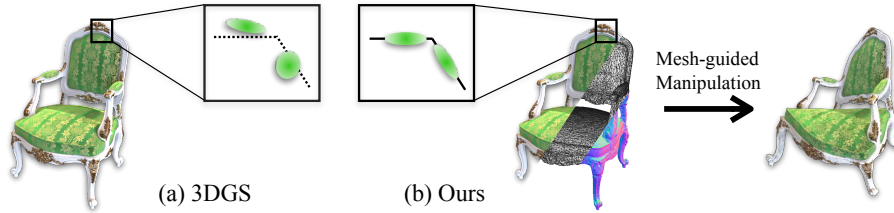


Fig. 1: The Gaussians and surface did not align well in the original 3DGS, whereas our hybrid representation explicitly restricts the Gaussians to the mesh faces. Our method benefits from the high-quality rendering of 3DGS and the controllability of a mesh.

the shape surface. As illustrated in Fig. 1, the Gaussians form an appearance model that may not accurately represent the geometry required by a mesh representation. Recently, some methods have incorporated regularization into the 3DGS learning process. NeuSG [3] refines Gaussians using surface normals estimated by a jointly trained NeuS model, which notably increases the training time. SuGaR [10] encourages Gaussians to align with the surface and subsequently treats the Gaussians as a point cloud for Poisson Surface Reconstruction. While these methods successfully extract a mesh, they require an additional step of training a new set of Gaussians bound to the mesh faces. This two-stage process brings inconvenience to existing downstream applications, including GS-Avatars [20], GS-VR [12], and physics simulations [6,8]. This limitation motivates us to design a more effective information pathway to supervise the learning of scene representations.

In this paper, we propose a novel approach that directly learns mesh and Gaussians from images in an end-to-end manner. Specifically, we utilize a differentiable marching module to extract a mesh, then derive Gaussians from the marched faces for strict alignment and employ the 3DGS workflow for rendering. We make the Gaussian covariances adaptive to irregular faces and use a neural network to robustly learn Gaussian colors as the mesh is jointly optimized. This resultant scene representation benefits from the rendering quality and efficiency of Gaussians, as well as the controllability of the mesh. Furthermore, the time required to extract a scene mesh is reduced to less than 2 hours on a single GPU, compared to other methods that rely on Neural SDFs and work on neural radiance fields [15,27], which require more than one day of training.

In summary, our contributions are as follows:

- We present a framework for directly learning scene representations with mesh and Gaussian-based appearance in an end-to-end manner, while ensuring explicit alignment and correspondence between Gaussians and mesh faces.
- We enhance the existing differentiable mesh extraction method to broaden its applicability to outdoor scenes.
- We introduce a scheme that adaptively adjusts the covariances of Gaussians based on their associated mesh faces and learns the colors of Gaussians

through a neural network, thereby enhancing the robustness of the optimization process.

Experimental results demonstrate that our method can efficiently extract a scene representation with explicit geometry and achieve high-quality rendering. Furthermore, we have showcased its application in scene modification and adaptation to scene updates.

2 Related Work

2.1 Scene Reconstruction via Radiance Field

Neural Radiance Field (NeRF) [17] is a significant advancement in 3D reconstruction. It uses neural networks to model the radiance field and yield high-fidelity images via volumetric rendering. Despite its outstanding rendering quality, NeRF requires a long time for training and rendering due to the large number of samples needed to query the neural network. Recent efforts to accelerate NeRF have employed explicit grids [7] or hybrids of grids and small MLPs [18, 24]. However, these computational accelerations might compromise image quality. In addition to improving speed, some works explore scene manipulation and composition within NeRF [30], but these are still not convenient for downstream applications. This has led to another series of works [26, 27] that connect NeRF with a mesh, which will be discussed in the next section.

Recently, 3D Gaussian Splatting (3DGS) [14] employs anisotropic Gaussians to model an explicit radiance field, achieving real-time rendering and enhanced quality. The explicit nature of 3DGS makes it suitable for various domains such as SLAM [13] and AIGC [5], where efficiency and controllability are crucial. However, directly manipulating 3DGS is challenging due to the vast number of Gaussian components involved. Hence, existing applications like Avatars [20], VR [12], and physics simulations [6, 8] leverage mesh guidance to manipulate the scene more effectively.

2.2 Image-based Surface Reconstruction

Reconstructing surfaces from images is a fundamental task in computer vision. Traditional methods, such as Multi-view Stereo (MVS) [2, 22], estimate depth maps or extract voxel grids based on correspondences between images. However, their quality is heavily dependent on the accuracy of image matching, and the use of voxel grids is often constrained by their cubic memory requirements. Recent advancements [19, 23] utilize differentiable isosurface extraction to directly optimize surface meshes under image supervision. Nonetheless, these methods are mainly for single objects due to the substantial memory demands of larger scenes.

Methods represented by NeuS [15, 27, 28] introduce a hybrid representation by transforming a Signed Distance Function (SDF) into a density field, adopting the learning pipeline of NeRFs. These techniques can model view-dependent

appearances and also allow for the extraction of meshes from the SDF, making them suitable for downstream applications. To enable real-time rendering, some approaches [21, 26, 31] bake the appearance from a trained NeRF into the mesh textures. However, they typically require extensive training times and might reduce rendering quality.

Several studies have achieved mesh extraction using 3DGS models. Dream-Gaussian [25] evaluates the density value of grid nodes using a mixture of neighborhood Gaussians and employs the Marching Cubes algorithm [16] to extract the isosurface. However, similar to NeRFs, the resulting density field may not accurately reflect the surface, leading to unsatisfactory surface quality in complex scenes. NeuSG [3] jointly learns NeuS and 3DGS models while introducing a regularization term to ensure consistency between the Gaussian orientation and the surface normal predicted by NeuS. This joint optimization significantly extends the training duration to over ten hours. Most recently, SuGaR [10] regularizes Gaussians using derived SDF values to align them with the surface and then treats the Gaussians as a point cloud for Poisson Surface Reconstruction. However, SuGaR requires the training of an additional set of Gaussians that are bound to the extracted mesh faces. In contrast, our approach simultaneously learns a hybrid representation of Gaussians and mesh from images.

3 Preliminary

3D Gaussian Splatting (3DGS) [14] uses a mixture of 3D Gaussians to model scene visuals. Each component is a Gaussian measure in 3D space, represented as $\exp\{-\frac{1}{2}(\mathbf{x} - \boldsymbol{\mu})^T \boldsymbol{\Sigma}^{-1}(\mathbf{x} - \boldsymbol{\mu})\}$, where $\boldsymbol{\mu}$ is the center position (mean) and $\boldsymbol{\Sigma}$ is the 3D covariance matrix. The visual information is characterized by opacity α and color \mathbf{c} , represented by spherical harmonics (SHs).

Physical properties that affect how a ray of light passes through the density field can be computed via integration through the density function. This naturally leads to an imaging model that can efficiently compute images based on Gaussian components by analytically solving the integration via projection:

$$\boldsymbol{\Sigma}' = \mathbf{J}\mathbf{W}\boldsymbol{\Sigma}\mathbf{W}^T\mathbf{J}^T, \quad (1)$$

where $\boldsymbol{\Sigma}'$ is the projected 2D covariance matrix, \mathbf{W} represents the current view-projection transformation, and \mathbf{J} is the Jacobian for an affine approximation to the projective transformation [32]. Additionally, the projected Gaussian center $\boldsymbol{\mu}'_i \in \mathbb{R}^2$ results from the standard projective transformation.

To query the color of a pixel of interest at location $\mathbf{x}' \in \mathbb{R}^2$, the sorted list of contributing Gaussians, \mathcal{N} , is determined based on their depths. The color of this pixel is then computed as follows:

$$\mathbf{C} = \sum_{i \in \mathcal{N}} \mathbf{c}_i \alpha'_i \prod_{j=1}^{i-1} (1 - \alpha'_j), \quad (2)$$

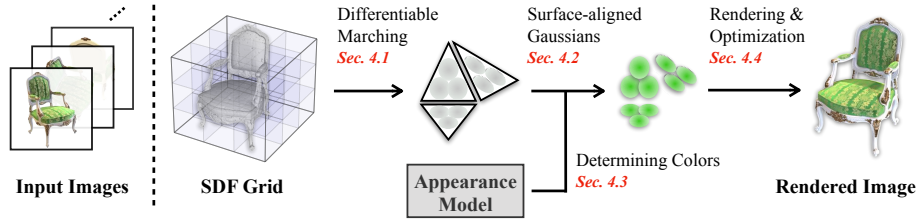


Fig. 2: Method Overview. The mesh is derived from a learnable SDF grid using a differentiable marching algorithm. Gaussians are created from the mesh faces, ensuring their alignment with the surface. A neural appearance model determines colors for Gaussians, which are then used to render an image.

where \mathbf{c}_i is the color of the i -th Gaussian, and α'_i is the opacity contributed by the Gaussian, computed by:

$$\alpha'_i = \alpha_i \times \exp \left\{ -\frac{1}{2} (\mathbf{x}' - \boldsymbol{\mu}'_i)^T \boldsymbol{\Sigma}'_i{}^{-1} (\mathbf{x}' - \boldsymbol{\mu}'_i) \right\}, \quad (3)$$

where α_i and $\boldsymbol{\mu}'_i$ denote the learnable opacity and the projected center of the i -th Gaussian, respectively.

Using images from known camera poses, the parameters of the Gaussian components are adjusted to align rendered and observed images. The optimization variables for covariance matrix $\boldsymbol{\Sigma}$ include a quaternion \mathbf{q} and a 3D vector \mathbf{s} , which relate to the objective through a change of variables:

$$\boldsymbol{\Sigma} = \mathbf{R} \mathbf{S} \mathbf{S}^T \mathbf{R}^T, \quad (4)$$

where \mathbf{R} and \mathbf{S} are the rotation and scaling matrices derived from \mathbf{q} and \mathbf{s} .

4 Method

The proposed method aims to obtain set of Gaussians that strictly align with object surfaces. These surfaces are constructed with triangle meshes, and the Gaussians are precisely defined in relation to the mesh faces. This method includes modular differentiable steps, allowing the model to learn from image observations as in original 3DGS.

An overview of our method is illustrated in Fig. 2. The components of the proposed learnable 3D scene model consist of: (1) a learnable SDF grid, whose nodes represent the signed distances to the surfaces in the scene; (2) a mesh derived from the SDF grid; (3) Gaussians bound to the simplices (triangles in this work) of the mesh; (4) an appearance field represented by a neural network.

In the model workflow, the relationships between these components are as follows: The mesh (2) is derived from the SDF grid (1) using a differentiable marching algorithm. The Gaussians (3) are then created and populated with queries to the network (4) for rendering an image, which is used to compute the photometric loss.

4.1 Differentiable Surface Extraction

The learnable Signed Distance Function (SDF) $s : \mathbb{R}^3 \mapsto \mathbb{R}$ is parameterized by scalar values at grid nodes $G = \{\mathbf{n}_i, \dots, \mathbf{n}_N\}$. We adopt the recently proposed FlexiCubes [23] as the differentiable surface extractor, which improves the original Marching Cubes algorithm by introducing learnable per-node deformations and weights for cell interpolation and quadrilateral splitting. This process yields a triangle mesh, characterized by vertices $\mathcal{V} = \{\mathbf{v}_1, \dots, \mathbf{v}_V\} \subset \mathbb{R}^3$ and faces $\mathcal{F} = \{\mathbf{f}_1, \dots, \mathbf{f}_F\}$, where each \mathbf{f} denotes a triplet of indices within $[1, \dots, V]$.

Existing differentiable marching methods are primarily used for single objects. A critical factor behind this limitation is the exponential increase in storage and computational demands required for processing all cells as the scene scope widens. To handle real-world indoor scenes and even outdoor scenes, we use three techniques as follows:

Foreground-Background Grids. We adopt two SDF grids to cover the pre-defined foreground and background domains, $D_{fg}, D_{bg} \subset \mathbb{R}^3$, respectively. Cells in the background grid located within D_{fg} are skipped during the marching procedure. For each training step, the resulting mesh is a composite of two meshes, each marched from one of the two grids.

Visible Node Optimization. As the camera only captures appearances within its current viewing frustum, it is unnecessary to extract mesh faces for the entire scene at each training iteration. Therefore, our focus shifts exclusively to the visible grid nodes, \hat{G} , calculated by:

$$\hat{G} = \{\mathbf{n} \in G \mid \text{NDC}(\mathbf{n}) \in [-1, 1]^3\} \quad (5)$$

where $\text{NDC}(\mathbf{n})$ is the transformation from world-space coordinates \mathbf{n} to their normalized device coordinates (NDC) via the projection matrix. The marching algorithm is only applied to cells whose eight corner nodes are within \hat{G} .

Coarse-to-fine Grid. Early use of a high-resolution grid in training often leads to numerous redundant faces, causing unstable learning and out-of-memory issues. Therefore, we start with a lower-resolution grid and increase the resolution several times (typically four times) during training until reaching the desired resolution. The enhancement of grid resolution is achieved through linear interpolation between the nodes of the existing grid and those of the refined grid. More details can be found in the appendix.

4.2 Explicitly Surface-aligned and Adaptive Gaussians

As shown in Fig. 3, we associate each triangular face with K Gaussians for a given extracted mesh $(\mathcal{V}, \mathcal{F})$. For a single face defined by vertices $\{\mathbf{v}_1, \mathbf{v}_2, \mathbf{v}_3\}$, the centers of the Gaussians are computed as follows:

$$\boldsymbol{\mu}_i = \mathbf{bc}_i[\mathbf{v}_1, \mathbf{v}_2, \mathbf{v}_3]^T, \quad i = 1, 2, \dots, K, \quad (6)$$

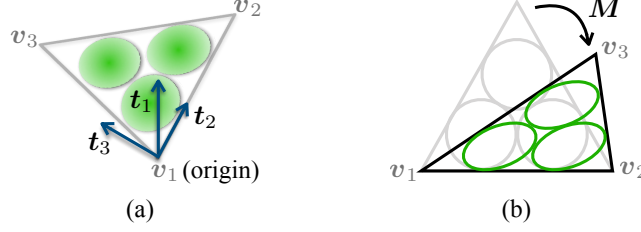


Fig. 3: Sub-figure (a) defines a local coordinate frame, while (b) illustrates applying linear transformation M to let Gaussians adapt to the irregular triangle. See Sec. 4.2 for more details.

where μ_i represents the center of the i -th Gaussian and bc_i denotes the predefined barycentric coordinates. The configurations of bc for different values of K are detailed in the appendix.

Before determining the Gaussian covariances, we introduce a local coordinate frame as illustrated in Fig. 3(a). This frame with origin at \mathbf{v}_1 comprises axes $\mathbf{t}_i = \tilde{\mathbf{t}}_i / \|\tilde{\mathbf{t}}_i\|$, $i \in \{1, 2, 3\}$, with:

$$\tilde{\mathbf{t}}_1 = \mathbf{a} \times \mathbf{b}, \quad \tilde{\mathbf{t}}_2 = \mathbf{a}, \quad \tilde{\mathbf{t}}_3 = (\mathbf{a} \times \mathbf{b}) \times \mathbf{a} \quad (7)$$

where $\mathbf{a} \equiv \mathbf{v}_2 - \mathbf{v}_1$, $\mathbf{b} \equiv \mathbf{v}_3 - \mathbf{v}_1$, and \times denotes the cross product. The rotation matrix from local space to world space is then $\mathbf{R}_{t2w} = [\mathbf{t}_1, \mathbf{t}_2, \mathbf{t}_3]$.

If the angles of a triangle are all close to $\pi/3$, the covariance matrix in the local coordinate frame can be naturally defined as $\Sigma_e = \text{diag}(\epsilon, r^2, r^2)$, representing a thin layer of Gaussian surrounding a small area of the surface. The choice of r is detailed in the appendix. For triangles with a more irregular aspect ratio, where the area is challenging to approximate by a disc, it is beneficial to linearly transform the Gaussian distribution with covariance Σ_e . Fig. 3(b) visualizes this transformation *within the local coordinate frame*. Here, the current triangle is denoted as $\mathbf{T} = [\mathbf{v}'_1, \mathbf{v}'_2, \mathbf{v}'_3]$, and the reference equilateral triangle as $\mathbf{E} = [\mathbf{v}'_1, \mathbf{v}'_2, \hat{\mathbf{v}}'_3]$, where \mathbf{v}'_i represents the local coordinates corresponding to \mathbf{v}_i , and $\hat{\mathbf{v}}'_3 = l * [0, \frac{1}{2}, \frac{\sqrt{3}}{2}]^T$, with $l = \|\mathbf{v}_2 - \mathbf{v}_1\|$.

By solving the equation $\mathbf{M}\mathbf{E} = \mathbf{T}$, we obtain:

$$\mathbf{M} = \begin{bmatrix} 1 & 0 & 0 \\ 0 & 1 & \frac{2\mathbf{v}'_3^{(2)} - l}{\sqrt{3}l} \\ 0 & 0 & \frac{2\mathbf{v}'_3^{(3)}}{\sqrt{3}l} \end{bmatrix}, \quad (8)$$

where $\mathbf{v}'_3^{(i)}$ denotes the i -th component of \mathbf{v}'_3 . The covariance matrix for the face Gaussians in world space is then given by:

$$\Sigma = \mathbf{R}_{t2w} \mathbf{M} \Sigma_e \mathbf{M}^T \mathbf{R}_{t2w}^T. \quad (9)$$

4.3 Gaussian Appearance Model

There are no direct connections between Gaussians derived from $(\mathcal{V}_t, \mathcal{F}_t)$ and those from $(\mathcal{V}_{t-1}, \mathcal{F}_{t-1})$, where t denotes the t -th training step. Hence, we are unable to optimize a constant group of per-Gaussian colors.

A straightforward approach would be to compute colors from neighboring Gaussians at the last step, formulated as $\mathbf{c}_{i,t} = \frac{1}{|\mathcal{N}|} \sum_{j \in \mathcal{N}} \mathbf{c}_{j,t-1}$, where $\mathbf{c}_{i,t}$ denotes the color of the i -th Gaussian at step t , and \mathcal{N} is the list of neighbors based on the Gaussian center. However, this method may require significant computation due to the neighbor search between two large sets of Gaussians. Additionally, averaging colors within a local region might lead to an over-smoothing issue.

To address these challenges, we introduce a volumetric appearance model, $\mathcal{A} : \mathbb{R}^3 \mapsto \mathbb{R}^D$, with D representing the color space dimension. At each step, we determine the color as $\mathbf{c} = \mathcal{A}(\boldsymbol{\mu})$ for the Gaussian centered at $\boldsymbol{\mu}$. To enhance efficiency and achieve a compact and continuous representation, we implement \mathcal{A} using hash-grid positional encoding [18] and a lightweight MLP, inspired by NvdiffrRec [19]. This appearance model can be robustly learned, even as the mesh changes from $(\mathcal{V}_{t-1}, \mathcal{F}_{t-1})$ to $(\mathcal{V}_t, \mathcal{F}_t)$.

Additionally, we set the opacity to $\alpha = 1$ to avoid semi-transparent faces.

4.4 Rendering and Optimization

As the Gaussians we construct retain the same form as those in the original 3DGS, we employ the same method defined in Eq. (2) for image rendering. Our method relies only on photometric supervision and utilizes the loss function:

$$\mathcal{L} = (1 - \lambda)\mathcal{L}_1 + \lambda\mathcal{L}_{D-SSIM}, \quad (10)$$

where λ is a weighting factor, and \mathcal{L}_1 , \mathcal{L}_{D-SSIM} represent standard L1 and D-SSIM metrics for comparing the rendered image against the ground truth.

Upon the convergence of the mesh and appearance model, we fix the topology defined by faces \mathcal{F} and proceed to jointly refine the vertices and the associated 3D Gaussians. During this phase, Gaussian centers continue to be derived from the face vertices using established barycentric coordinates. However, for covariance and color, we adopt a different approach since we can optimize a consistent set of Gaussian attributes during this phase. We sample the spherical harmonics (SHs) from the appearance model \mathcal{A} and make them a learnable, per-Gaussian variable as in the original 3DGS. Moreover, the Gaussian covariance is parameterized into learnable 2D scaling $\hat{\mathbf{s}} \in \mathbb{R}^2$ and a complex number $\mathbf{a}i + \mathbf{b}$ representing rotation, which are similar to the process in SuGaR [10]. It should be noted that this process is optional, as in many cases, the quality of the learned geometry and appearance without refinement is already satisfactory.

5 Experiments

In this section, we detail the implementation across different stages and describe the datasets used for evaluation.

To assess the effectiveness of our method, we compare it with models that specialize in novel view synthesis and surface reconstruction tasks, respectively. Note that the mesh is not used in the rendering of our method. Instead, it serves more as a constraint, ensuring that the Gaussians are aligned with the mesh to faithfully represent the geometry while also reproducing the scene’s appearance. We will demonstrate that, even with this constraint, our model can approximate or even surpass the performance of models without these constraints.

Furthermore, we showcase potential applications in object manipulation, and then discuss the adaptability to scene updates and ablation studies in the method analysis section.

5.1 Implementation details

The proposed method is implemented using PyTorch and the rasterization toolkit from 3DGS [14]. Experiments are conducted on an RTX A6000 GPU with 24GB memory. We will release source code upon acceptance of the paper.

Initialization. We train the original 3DGS model for 3,000 iterations to obtain a set of Gaussians, whose center positions are treated as a point cloud. We employ Alpha Shapes [4] to extract a coarse mesh and make it watertight [11]. In the next stage, we will construct an SDF grid based on this coarse mesh.

Our approach differs from others [19, 23] that randomly initialize the SDF, which would cause an OOM issue when the scene becomes large. Thanks to the fast optimization and the discrete nature of 3DGS, we are able to capture the coarse geometry within 5 minutes.

Joint Learning Mesh and Gaussians. The resolution of the used SDF grid depends on the scene. For Mip-NeRF360 scenes, we use 150^3 to 250^3 grid cells for the foreground and 250^3 to 300^3 for the background, placing 3 Gaussians for every marched face. For NeRF-Synthetic scenes, we use 100^3 grid cells and place 6 Gaussians on every face. For the appearance model, we adopt an MLP with 2 hidden layers, each comprising 32 neurons. This stage requires 10k iterations for optimization, totally using 15-50 minutes.

Refinement. The adaptive Gaussian binding strategy and appearance model enable mesh modifications within a specified range without impacting performance. Thus, we perform subdivision or decimation on the mesh to unify the number of faces (0.1M for single objects, 1.8M for real-world scenes) and then re-calculate the Gaussian covariances and colors. The refinement process consists of 7k iterations and requires 15-50 minutes.

5.2 Datasets and Metrics

The NeRF-Synthetic dataset [17] includes 8 scenes with 360° viewpoint settings of images. Besides testing novel view synthesis on this dataset, we quantitatively

Table 1: Per-scene quantitative comparisons on NeRF-Synthetic dataset [17].

Method	Chair			Drums			Ficus			Hotdog		
	PSNR↑	SSIM↑	LPIPS↓	PSNR↑	SSIM↑	LPIPS↓	PSNR↑	SSIM↑	LPIPS↓	PSNR↑	SSIM↑	LPIPS↓
without mesh												
NeRF [17]	33.00	0.967	0.046	25.01	0.925	0.091	30.13	0.964	0.044	36.18	0.974	0.121
Plenoxels [7]	33.98	0.977	0.031	25.35	0.933	0.067	31.83	0.976	0.026	36.43	0.980	0.037
3DGS [14]	35.82	0.987	0.012	26.17	0.954	0.037	34.83	0.987	0.012	37.67	0.985	0.020
with mesh												
NVdiffRec [19]	31.60	0.969	0.034	24.10	0.916	0.065	30.88	0.970	0.041	33.04	0.973	0.033
NeuManifold [29]	34.39	0.981	0.014	25.39	0.939	0.072	31.91	0.978	0.028	35.69	0.979	0.036
NeRF2Mesh [26]	34.25	0.978	0.031	25.04	0.926	0.084	30.08	0.967	0.046	35.70	0.974	0.058
Ours	35.56	0.986	0.013	25.78	0.949	0.044	33.51	0.984	0.015	36.41	0.983	0.021
Method	Lego			Materials			Mic			Ship		
	PSNR↑	SSIM↑	LPIPS↓	PSNR↑	SSIM↑	LPIPS↓	PSNR↑	SSIM↑	LPIPS↓	PSNR↑	SSIM↑	LPIPS↓
without mesh												
NeRF [17]	32.54	0.961	0.050	29.62	0.949	0.063	32.91	0.980	0.028	28.65	0.856	0.206
Plenoxels [7]	34.10	0.975	0.028	29.14	0.949	0.057	33.26	0.985	0.015	29.62	0.890	0.134
3DGS [14]	35.69	0.983	0.016	30.00	0.960	0.034	35.34	0.991	0.006	30.87	0.907	0.106
with mesh												
NVdiffRec [19]	29.14	0.949	0.042	26.74	0.923	0.060	30.78	0.977	0.024	26.12	0.833	0.080
NeuManifold [29]	34.00	0.977	0.024	26.69	0.924	0.115	33.40	0.986	0.012	28.63	0.875	0.168
NeRF2Mesh [26]	34.90	0.977	0.025	26.26	0.906	0.111	32.63	0.979	0.038	29.47	0.875	0.138
Ours	34.48	0.980	0.018	28.81	0.953	0.039	35.44	0.992	0.007	28.58	0.882	0.124

evaluate reconstructed surfaces using the provided ground-truth mesh. We also evaluate our method on 7 of the 9 real-world scenes in the Mip-NeRF360 dataset [1], excluding *Flowers* and *Treehill* due to licensing restrictions. The strategy for splitting subsets for training and testing follows that of 3DGS [14].

For novel view synthesis, we employ the standard PSNR, L-PIPS, and SSIM metrics. In the surface reconstruction task, we compute the Chamfer Distance (CD) between the extracted mesh and the ground truth.

5.3 Novel View Synthesis

We first evaluate our method on the novel view synthesis task. Tabs. 1 and 2 present the quantitative results on NeRF-Synthetic and Mip-NeRF360 datasets. To ensure a fair comparison, we employed a white background for the NeRF-Synthetic dataset. Our approach is compared against various recent methods, including those with reconstructed mesh and those without.

For the NeRF-Synthetic dataset, our method achieves state-of-the-art rendering quality among methods reconstructing a mesh, and even outperforms some models that solely focus on rendering quality. Furthermore, there is only a slight decrease in performance compared to the original 3DGS. For the Mip-NeRF360 dataset, our method is comparable to the state-of-the-art method [10]. In some cases (e.g., *bicycle*), our method achieves better geometric correctness, even if the PSNR for those scenes is not as high as SuGaR’s. This phenomenon is demonstrated by the qualitative comparison in Fig. 4.

Table 2: Quantitative comparisons on Mip-NeRF360 dataset [1].

Method	Indoor scenes			Outdoor scenes			All scenes		
	PSNR \uparrow	SSIM \uparrow	LPIPS \downarrow	PSNR \uparrow	SSIM \uparrow	LPIPS \downarrow	PSNR \uparrow	SSIM \uparrow	LPIPS \downarrow
without mesh									
Plenoxels [7]	24.83	0.766	0.426	22.02	0.542	0.465	23.62	0.670	0.443
INGP-Base [18]	28.65	0.840	0.281	23.47	0.571	0.416	26.43	0.725	0.339
3DGS [14]	30.41	0.920	0.189	26.40	0.805	0.173	28.69	0.870	0.182
with mesh									
NeRFMeshing [21]	23.83	-	-	22.23	-	-	23.15	-	-
BakedSDF [31]	27.06	0.836	0.258	-	-	-	-	-	-
NeuManifold [29]	27.16	0.813	0.316	-	-	-	-	-	-
NeRF2Mesh [26]	-	-	-	22.74	0.523	0.457	-	-	-
SuGaR-15K [10]	29.43	0.910	0.216	24.40	0.699	0.301	27.27	0.820	0.253
Ours	29.06	0.908	0.198	23.80	0.665	0.274	26.80	0.804	0.230

Table 3: Mesh quality evaluation. Chamfer Distance (CD) are compared to the ground truth meshes from NeRF-Synthetic dataset.

Method	CD (10^{-3})	#Faces	PSNR
NVdiffRec [19]	8.15	80k	29.05
NeRF2Mesh [26]	5.06	192k	31.04
Ours	7.27	100k	32.32

5.4 Surface Reconstruction

Although our focus is on establishing a hybrid representation that ensures alignment between Gaussians and mesh faces, the surfaces reconstructed by our method are of good quality. We visualize the reconstructed meshes and their normal maps in Fig. 5, which demonstrates that our method effectively captures the surface details of a scene. More results can be found in the appendix.

For a quantitative evaluation of the meshes, we compare the reconstructed mesh to the ground truth from the NeRF-Synthetic dataset using the Chamfer Distance (CD) metric. The computation method follows NeRF2Mesh [26], where 2.5M points are sampled from the surfaces of both the ground truth and the reconstructed object through ray casting. Tab. 3 presents the CD results, the number of faces, and the rendering PSNR, illustrating that our resultant meshes achieve high quality in quantitative measures. Furthermore, the Gaussian-based appearance enables high-quality rendering even with fewer faces than NeRF2Mesh.

5.5 Object Deformation by Hybrid Representation

As discussed in our introduction section, the hybrid representation not only benefits from the high-quality and efficient rendering of Gaussians but also offers

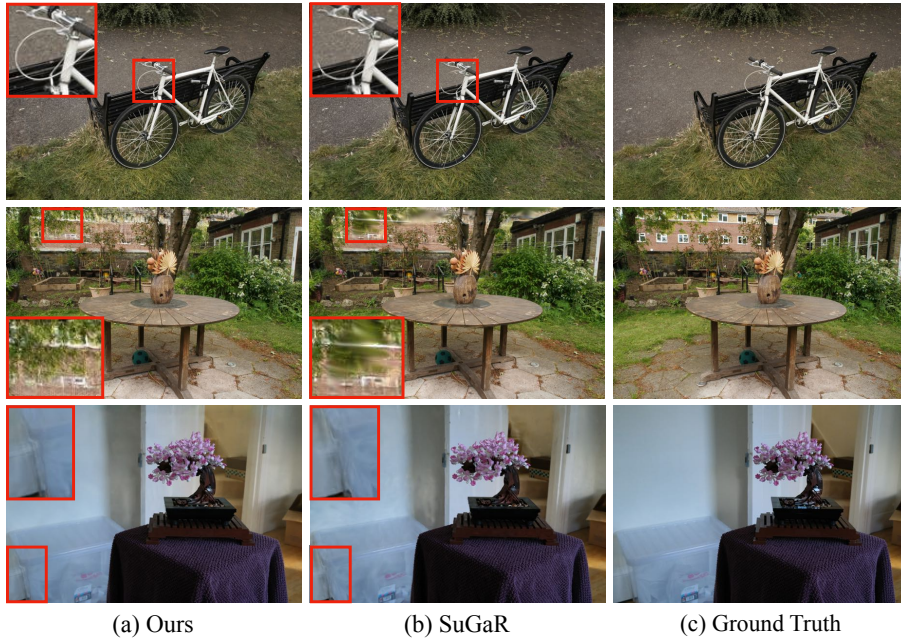


Fig. 4: Qualitative comparisons with SuGaR [10] on the Mip-NeRF360 dataset [1].

Table 4: Ablation studies. We conduct evaluations on the Mip-NeRF360 dataset [1] and report the average PSNR across all scenes.

Adaptive Covariance	Refinement	PSNR	GS/face	PSNR	Time
×	✓	26.53	1	26.53	1.5h
✓	×	23.77	3	26.80	2h
✓	✓	26.80	6	26.87	2.5h

the convenience of manipulation through the mesh. To demonstrate the potential applications of this work, we selected object deformation tasks for testing. Specifically, we deform the learned mesh using four common mesh modifiers (Twist, Stretch, Bend, and Taper) in Blender and correspondingly adjust the bound Gaussians using the technique described in Sec. 4.2. We then use the Gaussian-based rasterization to render images of the deformed object, as shown in Fig. 6. More advanced operations, as explored in [9, 12], have been examined and are also compatible with the representation we have obtained.

5.6 Method Analysis

Adaptability in Scene Updates. One unique feature of our method is the simultaneous learning of topology (defined by mesh faces) and Gaussians. In

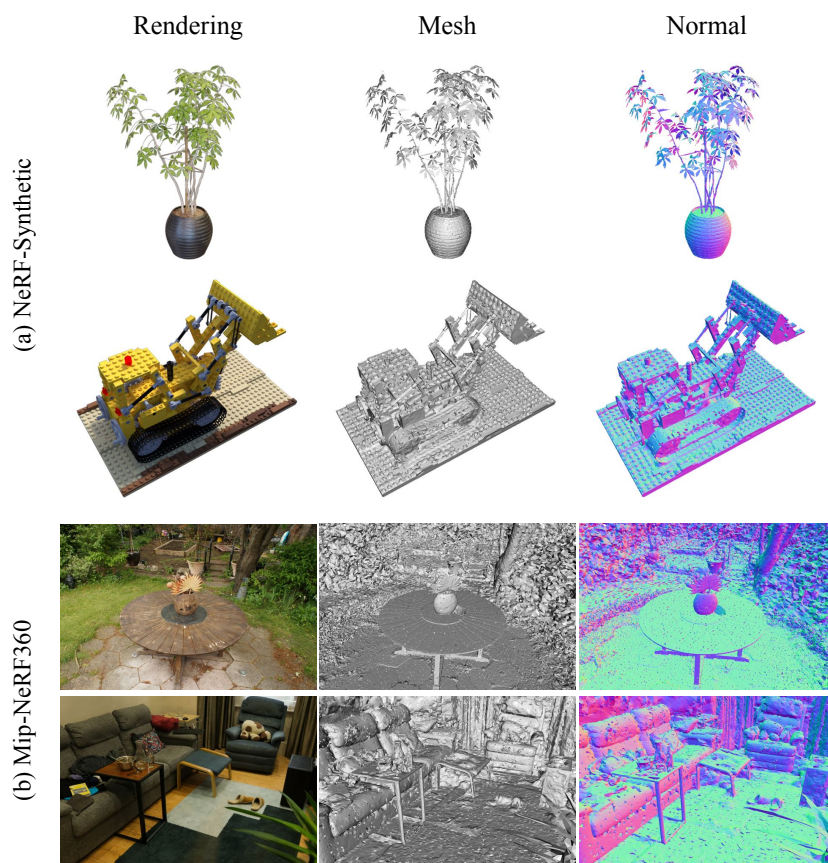


Fig. 5: Rendered images and reconstructed meshes on NeRF-Synthetic [17] and Mip-NeRF360 [1] datasets.



Fig. 6: Object deformation by hybrid representation of mesh and Gaussians. We employ four Blender modifiers to manipulate the mesh, subsequently render perspectives using the bound Gaussians.

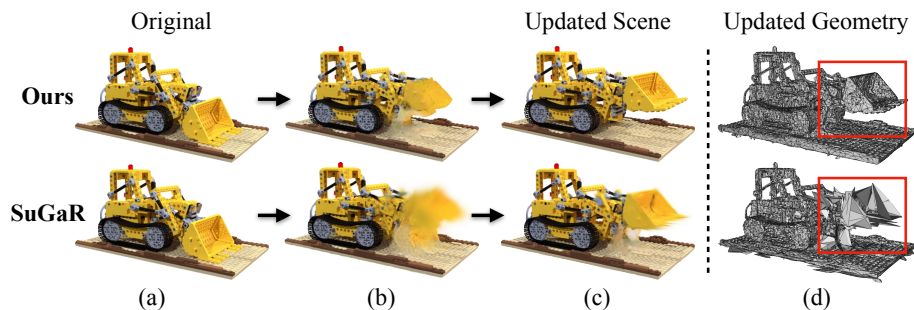


Fig. 7: Adaptation to scene updates. (a) Models initially trained on the original scene. (b) and (c): Models adapted to the updated scene for 500 and 5000 steps, respectively. (d): The meshes learned on the updated scene.

contrast, the existing method, SuGaR [10], separates the learning of topology and Gaussians, as the mesh extraction process (Poisson Surface Reconstruction) is non-differentiable for Gaussian rasterization.

In practice, when part of the scene requires updating, our model can directly adapt to these changes without re-learning from scratch. Fig. 7 presents the results of dealing with scene updates using our method and SuGaR. Our method successfully updates the geometry and appearances of the updated regions, while SuGaR struggles to adapt to new scene geometries with its fixed topology.

Ablation Studies. In this section, we examine the impact of three factors: 1) the adaptive Gaussian covariance; 2) the refinement stage; and 3) the number of Gaussians per face. For evaluating the adaptive Gaussian covariance, we set M in Eq. (9) to be an identity matrix.

Tab. 4 presents results from the Mip-NeRF360 dataset, showing that both adaptive Gaussian covariance and the refinement stage significantly enhance performance. Additionally, increasing the number of Gaussians per face is beneficial for rendering quality but leads to a longer training time. As a trade-off, we use only 3 Gaussians per face in this paper.

6 Conclusion

We have proposed a novel learning method to capture comprehensive 3D scene information from multiple views. The method simultaneously extracts both the geometry and the physical properties affecting the observed appearance. The geometry is extracted in the explicit form of triangle meshes. The appearance properties are encoded in 3D Gaussians that are bound to the mesh faces. Thanks to the 3DGS-based differentiable rendering, we are able to establish an effective and efficient learning procedure by directly optimizing the photometric loss. Experiments verify that the resulting representation enjoys both high-quality rendering and controllability.

References

1. Barron, J.T., Mildenhall, B., Verbin, D., Srinivasan, P.P., Hedman, P.: Mip-nerf 360: Unbounded anti-aliased neural radiance fields. In: IEEE/CVF Conference on Computer Vision and Pattern Recognition, CVPR 2022, New Orleans, LA, USA, June 18-24, 2022. pp. 5460–5469. IEEE (2022) [10](#), [11](#), [12](#), [13](#)
2. Bleyer, M., Rhemann, C., Rother, C.: Patchmatch stereo - stereo matching with slanted support windows. In: Hoey, J., McKenna, S.J., Trucco, E. (eds.) British Machine Vision Conference, BMVC 2011, Dundee, UK, August 29 - September 2, 2011. Proceedings. pp. 1–11. BMVA Press (2011) [3](#)
3. Chen, H., Li, C., Lee, G.H.: Neusg: Neural implicit surface reconstruction with 3d gaussian splatting guidance. CoRR [abs/2312.00846](#) (2023) [2](#), [4](#)
4. Edelsbrunner, H., Kirkpatrick, D.G., Seidel, R.: On the shape of a set of points in the plane. IEEE Trans. Inf. Theory **29**(4), 551–558 (1983) [9](#)
5. Fang, J., Wang, J., Zhang, X., Xie, L., Tian, Q.: Gaussianeditor: Editing 3d gaussians delicately with text instructions. CoRR [abs/2311.16037](#) (2023) [3](#)
6. Feng, Y., Feng, X., Shang, Y., Jiang, Y., Yu, C., Zong, Z., Shao, T., Wu, H., Zhou, K., Jiang, C., Yang, Y.: Gaussian splashing: Dynamic fluid synthesis with gaussian splatting. CoRR [abs/2401.15318](#) (2024) [2](#), [3](#)
7. Fridovich-Keil, S., Yu, A., Tancik, M., Chen, Q., Recht, B., Kanazawa, A.: Plenoxels: Radiance fields without neural networks. In: IEEE/CVF Conference on Computer Vision and Pattern Recognition, CVPR 2022, New Orleans, LA, USA, June 18-24, 2022. pp. 5491–5500. IEEE (2022) [3](#), [10](#), [11](#)
8. Gao, L., Yang, J., Zhang, B.T., Sun, J.M., Yuan, Y.J., Fu, H., Lai, Y.K.: Mesh-based gaussian splatting for real-time large-scale deformation. CoRR [abs/2402.04796](#) (2024) [2](#), [3](#)
9. Gao, L., Yang, J., Zhang, B., Sun, J., Yuan, Y., Fu, H., Lai, Y.: Mesh-based gaussian splatting for real-time large-scale deformation. CoRR [abs/2402.04796](#) (2024) [12](#)
10. Guédon, A., Lepetit, V.: Sugar: Surface-aligned gaussian splatting for efficient 3d mesh reconstruction and high-quality mesh rendering. CoRR [abs/2311.12775](#) (2023) [2](#), [4](#), [8](#), [10](#), [11](#), [12](#), [14](#)
11. Huang, J., Su, H., Guibas, L.J.: Robust watertight manifold surface generation method for shapenet models. CoRR [abs/1802.01698](#) (2018) [9](#)
12. Jiang, Y., Yu, C., Xie, T., Li, X., Feng, Y., Wang, H., Li, M., Lau, H.Y.K., Gao, F., Yang, Y., Jiang, C.: VR-GS: A physical dynamics-aware interactive gaussian splatting system in virtual reality. CoRR [abs/2401.16663](#) (2024) [2](#), [3](#), [12](#)
13. Keetha, N.V., Karhade, J., Jatavallabhula, K.M., Yang, G., Scherer, S.A., Ramanan, D., Luiten, J.: Splatam: Splat, track & map 3d gaussians for dense RGB-D SLAM. CoRR [abs/2312.02126](#) (2023) [3](#)
14. Kerbl, B., Kopanas, G., Leimkühler, T., Drettakis, G.: 3d gaussian splatting for real-time radiance field rendering. ACM Trans. Graph. **42**(4), 139:1–139:14 (2023) [1](#), [3](#), [4](#), [9](#), [10](#), [11](#)
15. Li, Z., Müller, T., Evans, A., Taylor, R.H., Unberath, M., Liu, M., Lin, C.: Neuralangelo: High-fidelity neural surface reconstruction. In: IEEE/CVF Conference on Computer Vision and Pattern Recognition, CVPR 2023, Vancouver, BC, Canada, June 17-24, 2023. pp. 8456–8465. IEEE (2023) [2](#), [3](#)
16. Lorensen, W.E., Cline, H.E.: Marching cubes: A high resolution 3d surface construction algorithm. In: Stone, M.C. (ed.) Proceedings of the 14th Annual Conference on Computer Graphics and Interactive Techniques, SIGGRAPH 1987, Anaheim, California, USA, July 27-31, 1987. pp. 163–169. ACM (1987) [4](#)

17. Mildenhall, B., Srinivasan, P.P., Tancik, M., Barron, J.T., Ramamoorthi, R., Ng, R.: Nerf: Representing scenes as neural radiance fields for view synthesis. In: Vedaldi, A., Bischof, H., Brox, T., Frahm, J. (eds.) *Computer Vision - ECCV 2020 - 16th European Conference, Glasgow, UK, August 23-28, 2020, Proceedings, Part I*. Lecture Notes in Computer Science, vol. 12346, pp. 405–421. Springer (2020) [1](#), [3](#), [9](#), [10](#), [13](#)
18. Müller, T., Evans, A., Schied, C., Keller, A.: Instant neural graphics primitives with a multiresolution hash encoding. *ACM Trans. Graph.* **41**(4), 102:1–102:15 (2022) [3](#), [8](#), [11](#)
19. Munkberg, J., Chen, W., Hasselgren, J., Evans, A., Shen, T., Müller, T., Gao, J., Fidler, S.: Extracting triangular 3d models, materials, and lighting from images. In: *IEEE/CVF Conference on Computer Vision and Pattern Recognition, CVPR 2022, New Orleans, LA, USA, June 18-24, 2022*. pp. 8270–8280. IEEE (2022) [3](#), [8](#), [9](#), [10](#), [11](#)
20. Qian, S., Kirschstein, T., Schoneveld, L., Davoli, D., Giebenhain, S., Nießner, M.: Gaussianavatars: Photorealistic head avatars with rigged 3d gaussians. *CoRR* **abs/2312.02069** (2023) [2](#), [3](#)
21. Rakotosaona, M., Manhardt, F., Arroyo, D.M., Niemeyer, M., Kundu, A., Tombari, F.: Nerfmeshing: Distilling neural radiance fields into geometrically-accurate 3d meshes. *CoRR* **abs/2303.09431** (2023) [4](#), [11](#)
22. Schönberger, J.L., Zheng, E., Frahm, J., Pollefeys, M.: Pixelwise view selection for unstructured multi-view stereo. In: Leibe, B., Matas, J., Sebe, N., Welling, M. (eds.) *Computer Vision - ECCV 2016 - 14th European Conference, Amsterdam, The Netherlands, October 11-14, 2016, Proceedings, Part III*. Lecture Notes in Computer Science, vol. 9907, pp. 501–518. Springer (2016) [3](#)
23. Shen, T., Munkberg, J., Hasselgren, J., Yin, K., Wang, Z., Chen, W., Gojcic, Z., Fidler, S., Sharp, N., Gao, J.: Flexible isosurface extraction for gradient-based mesh optimization. *ACM Trans. Graph.* **42**(4), 37:1–37:16 (2023) [3](#), [6](#), [9](#)
24. Sun, C., Sun, M., Chen, H.: Direct voxel grid optimization: Super-fast convergence for radiance fields reconstruction. In: *IEEE/CVF Conference on Computer Vision and Pattern Recognition, CVPR 2022, New Orleans, LA, USA, June 18-24, 2022*. pp. 5449–5459. IEEE (2022) [3](#)
25. Tang, J., Ren, J., Zhou, H., Liu, Z., Zeng, G.: Dreamgaussian: Generative gaussian splatting for efficient 3d content creation. *CoRR* **abs/2309.16653** (2023) [4](#)
26. Tang, J., Zhou, H., Chen, X., Hu, T., Ding, E., Wang, J., Zeng, G.: Delicate textured mesh recovery from nerf via adaptive surface refinement. In: *IEEE/CVF International Conference on Computer Vision, ICCV 2023, Paris, France, October 1-6, 2023*. pp. 17693–17703. IEEE (2023) [3](#), [4](#), [10](#), [11](#)
27. Wang, P., Liu, L., Liu, Y., Theobalt, C., Komura, T., Wang, W.: Neus: Learning neural implicit surfaces by volume rendering for multi-view reconstruction. In: Ranzato, M., Beygelzimer, A., Dauphin, Y.N., Liang, P., Vaughan, J.W. (eds.) *Advances in Neural Information Processing Systems 34: Annual Conference on Neural Information Processing Systems 2021, NeurIPS 2021, December 6-14, 2021, virtual*. pp. 27171–27183 (2021) [1](#), [2](#), [3](#)
28. Wang, Y., Han, Q., Habermann, M., Daniilidis, K., Theobalt, C., Liu, L.: Neus2: Fast learning of neural implicit surfaces for multi-view reconstruction. In: *IEEE/CVF International Conference on Computer Vision, ICCV 2023, Paris, France, October 1-6, 2023*. pp. 3272–3283. IEEE (2023) [3](#)
29. Wei, X., Xiang, F., Bi, S., Chen, A., Sunkavalli, K., Xu, Z., Su, H.: Neumanifold: Neural watertight manifold reconstruction with efficient and high-quality rendering support. *CoRR* **abs/2305.17134** (2023) [10](#), [11](#)

30. Yang, B., Zhang, Y., Xu, Y., Li, Y., Zhou, H., Bao, H., Zhang, G., Cui, Z.: Learning object-compositional neural radiance field for editable scene rendering. In: 2021 IEEE/CVF International Conference on Computer Vision, ICCV 2021, Montreal, QC, Canada, October 10-17, 2021. pp. 13759–13768. IEEE (2021) [3](#)
31. Yariv, L., Hedman, P., Reiser, C., Verbin, D., Srinivasan, P.P., Szeliski, R., Barron, J.T., Mildenhall, B.: Baked sdf: Meshing neural sdfs for real-time view synthesis. In: Brunvand, E., Sheffer, A., Wimmer, M. (eds.) ACM SIGGRAPH 2023 Conference Proceedings, SIGGRAPH 2023, Los Angeles, CA, USA, August 6-10, 2023. pp. 46:1–46:9. ACM (2023) [1](#), [4](#), [11](#)
32. Zwicker, M., Pfister, H., van Baar, J., Gross, M.H.: EWA volume splatting. In: Ertl, T., Joy, K.I., Varshney, A. (eds.) 12th IEEE Visualization Conference, IEEE Vis 2001, San Diego, CA, USA, October 24-26, 2001, Proceedings. pp. 29–36. IEEE Computer Society (2001) [4](#)